

RESEARCH ARTICLE

A fully three-dimensional kinetic particle-in-cell framework for modeling laser–dielectric interactions: few-cycle pulse damage

Joseph R. Smith¹, Ziyao Su², Simin Zhang², Charles Varin³, Vitaly E. Gruzdev⁴, and Enam A. Chowdhury^{2,5,6}

¹Department of Physics, Marietta College, Marietta, Ohio, USA

²Department of Materials Science and Engineering, The Ohio State University, Columbus, Ohio, USA

³Cégep de l'Outaouais - CyberQuébec, Gatineau, Canada

⁴Department of Physics and Astronomy, University of New Mexico, Albuquerque, New Mexico, USA

⁵Department of Electrical and Computer Engineering, The Ohio State University, Columbus, Ohio, USA

⁶Department of Physics, The Ohio State University, Columbus, Ohio, USA

(Received 4 March 2025; revised 25 April 2025; accepted 5 June 2025)

Abstract

We present a fully three-dimensional kinetic framework for modeling intense short pulse lasers interacting with dielectric materials. Our work modifies the open-source particle-in-cell code EPOCH to include new models for photoionization and dielectric optical response. We use this framework to model the laser-induced damage of dielectric materials by few-cycle laser pulses. The framework is benchmarked against experimental results for bulk silica targets and then applied to model multi-layer dielectric mirrors with a sequence of simulations with varying laser fluence. This allows us to better understand the laser damage process by providing new insight into energy absorption, excited particle dynamics and nonthermal excited particle distributions. We compare common damage threshold metrics based on the energy density and excited electron density.

Keywords: laser induced damage threshold; particle in cell; few-cycle pulse; laser damage simulation; multi-layer dielectric mirrors

1. Introduction

The 2023 Nobel Prize in Physics awarded to Pierre Agostini, Ferenc Krausz and Anne L'Huillier 'for experimental methods that generate attosecond pulses of light for the study of electron dynamics in matter'^[1] and the 2018 National Academies of Science report^[2] that spurred the 'Brightest Light Initiative'^[3] highlight the impactful science enabled by producing the shortest possible pulses of light^[4–6]. Recent advances in high-energy few-cycle pulse generation techniques^[7,8] allow us to probe new physical effects, including those from the carrier-envelope phase^[9–11], and to generate high laser intensities with moderate laser energies for applications such as relativistic plasma-based attosecond pulse generation^[12]. These developments motivate the design of optical components with higher laser-induced damage

thresholds (LIDTs) for few- to single-cycle pulses. The scaling of LIDTs with laser fluence is generally well understood for the tens of picosecond to nanosecond regimes^[13], but is more complex for shorter pulses^[14], especially few-cycle pulses^[15,16].

Previous experimental work has explored the damage and ablation of SiO₂ using few-cycle approximately 800 nm wavelength pulses with durations of 5 fs^[15,17,18] and 7 fs^[16,19–21]. Recently Kafka *et al.*^[18] determined the damage threshold for different optical components with a 5 fs pulse and Talisa *et al.*^[22] explored the damage and ablation of SiO₂/HfO₂ multi-layer coatings with 8 fs pulses. As highlighted in the review by Nagy *et al.*^[8], post-compression techniques allow researchers around the world (e.g., Refs. [12,23–25]) to generate few-cycle pulses, but traditional optics are easily damaged by these compressed pulses.

Understanding few-cycle pulse material interactions requires advances in computational and theoretical models. There has been significant work using one-dimensional finite-difference-time-domain (FDTD) simulations to model these interactions^[26], with recent efforts in two

Correspondence to: J. R. Smith, Department of Physics, Marietta College, Marietta, Ohio 45750, USA. Email: JosephRSmith@protonmail.com. E. A. Chowdhury, Department of Materials Science and Engineering, The Ohio State University, Columbus, Ohio 43210, USA. Email: chowdhury.24@osu.edu

dimensions^[27,28]. FDTD simulations provide insight into the laser material interactions and can predict LIDTs, but do not capture the nonthermal nature of excited electrons, nor do they capture their ballistic motion. To expand our understanding of the interaction dynamics, we use particle-in-cell (PIC) simulations^[29,30]. As with FDTD simulations, PIC codes solve Maxwell's equations on a computational grid. In addition, PIC simulations statistically represent the neutral and excited particles in the simulation with a finite number of 'macroparticles'^[29–31]. The charged particles are then advanced using the Lorentz force and additional physical effects, including ionization and collisions, are often added.

PIC simulations are commonly used to study laser–plasma interactions (e.g., by Ziegler *et al.*^[32]) and are increasingly being modified to simulate laser damage and related regimes. For example, Mitchell *et al.*^[33] modeled crater formation in metals due to femtosecond laser ablation, Cochran *et al.*^[34] modeled liquid-crystal plasma mirrors^[35], Déziel *et al.*^[36] studied laser-induced periodic surface structures and Ding *et al.*^[37] and Do *et al.*^[38] modeled plasmons using PIC simulations. Interactions of lasers with nano/micro-scale structures in silicon and SiO₂ have been modeled with versions of the framework introduced in this work^[39,40] and recently Charpin *et al.*^[41] developed a similar framework to explore ionization in dielectrics. Our work builds on these efforts specifically for laser damage for few-cycle pulses by including the corrected Keldysh ionization model^[28,42,43] to account for ionization across a range of fluences. We are able to explore the nonthermal distribution of excited particles in the laser damage regime using PIC simulation, which improves our fundamental understanding of damage mechanisms.

In this work, we begin in Section 2 by introducing the modifications and extensions we have made to a PIC code to model laser–dielectric interactions. Then in Section 3 we discuss the material properties and simulation setup for both bulk and multi-layer targets. Next, in Section 4 we compare the predictions of this framework to existing experimental results and discuss expected damage threshold metrics. Then we apply the framework to the modeling of multi-layer mirrors in Section 5 and conclude in Section 6.

2. Particle-in-cell simulation modifications

Our work extends the three-dimensional (3D) implementation of version 4.17.10 of the EPOCH^[31] PIC code, which is designed for the study of high-energy-density physics. EPOCH is a popular open-source PIC code that can scale to run on thousands of central processing unit (CPU) cores, although we note that there are a variety of other open-source and proprietary PIC codes available with different features and implementations^[44], such as graphics processing unit (GPU) operation (e.g., PIConGPU^[45] and WarpX^[46]). PIC simulations of laser–matter interactions are typically used to

study only tens-to-hundreds of femtosecond timescales due to numerical instability issues and computational cost. As such, we focus on the initial laser–matter interaction and the resulting excited electron dynamics. For long-term dynamics and equilibration, one could use a final simulation state from a PIC model as the initial conditions for another model. For example, one could use the electron and ion temperatures in a two-temperature model, or consider tabulated equation of state values^[16].

EPOCH includes multiple physics modules, but was not designed with laser–dielectric interactions in mind. Towards this goal, we have added a new photoionization model relevant for dielectric materials and a model for optical material properties, as discussed in the next sections.

2.1. Keldysh photoionization

Our work extends the existing ionization framework already available in EPOCH^[31] to include the photoionization model developed by Keldysh^[42]. The Keldysh ionization model allows us to calculate probabilities for electron transitions from the valence to the conduction band in solids due to the electric field of a laser pulse^[47].

For a laser pulse with electric field amplitude E and frequency ω interacting with a material having band gap Δ and reduced electron-hole mass m^* , the Keldysh parameter is $\gamma = \omega\sqrt{m^*}\Delta/eE$, where $\gamma \gg 1$ is for the multiphoton ionization regime and $\gamma \ll 1$ is for the tunneling regime^[42]. The Keldysh formulation is especially useful as it spans both regimes, which are often present when considering a laser-induced damage experiment. For example, the peak electric fields in our simulations give values of γ ranging from about 0.3 to 0.9, which means the photoionization regime is neither multiphoton nor tunneling, suggesting that the full Keldysh formula should be utilized.

The Keldysh model is used in our simulations to calculate the probability that a given neutral macroparticle will ionize. When ionization occurs, a new electron macroparticle and corresponding ion macroparticle are created in place of the original macroparticle. Now we introduce the ionization rate equation used in our work. For brevity in the following expressions, we follow Refs. [48,49] by introducing the variables $\gamma_1 = \gamma^2/(1 + \gamma^2)$ and $\gamma_2 = 1/(1 + \gamma^2)$. The effective band gap is then given by the following:

$$x = \frac{2}{\pi} \frac{\Delta}{\hbar\omega} \frac{\epsilon(\gamma_2)}{\sqrt{\gamma_1}}. \quad (1)$$

We may then write the ionization rate W as follows:

$$W [\text{m}^{-3}\text{s}^{-1}] = 2 \frac{2\omega}{9\pi} \left(\frac{m^*\omega}{\hbar\sqrt{\gamma_1}} \right)^{3/2} \times Q(\gamma, x) \exp \left(-\pi [x + 1] \frac{\kappa(\gamma_1) - \epsilon(\gamma_1)}{\epsilon(\gamma_2)} \right), \quad (2)$$

where κ and ϵ are complete elliptic integrals of the first and second kind, Φ is the Dawson integral and

$$Q(\gamma, x) = \sqrt{\frac{\pi}{2\kappa(\gamma_2)}} \sum_{n=0}^{\infty} \exp\left(-n\pi \frac{\kappa(\gamma_1) - \epsilon(\gamma_1)}{\epsilon(\gamma_2)}\right) \times \Phi\left(\sqrt{\frac{\pi^2 (\lfloor x+1 \rfloor - x + n)}{2\kappa(\gamma_2)\epsilon(\gamma_2)}}\right). \quad (3)$$

We note that this is the corrected version of the formulation, where the original contains a misprint as noted by Gruzdev^[43]. Using the uncorrected version can result in significantly different calculations^[28,43].

For our simulation framework, the Keldysh ionization rate is evaluated *in situ* (with the exception of the elliptic integrals, which are read from tabulated data files with 1000 points) rather than interpolated from a tabulated form, which facilitates accuracy over a wide range of fluences. We use the first 500 terms in this infinite sum in Equation (3), which is sufficient for the regimes of interest in this paper, as illustrated in the appendix, while limiting the computational cost. An adaptive approach to a prescribed tolerance could be employed in the future. Currently each macroparticle can only be ionized once.

While the Keldysh parameter depends on the laser amplitude E , the amplitudes of our pulses vary within the laser envelope. Moreover, each computational cell in a PIC simulation only considers the instantaneous electric field. To address this, we store the electric field magnitude at each time step using an array large enough to store an entire laser cycle on a rolling window, as suggested by Zhang *et al.*^[28]. Then the maximum field for the previous cycle is used to approximate the amplitude to calculate the ionization rate. This approach would encounter challenges for single-cycle pulses. In the future a more complex envelope model could be explored^[50].

2.2. Collisional effects

We use the Pérez/Nambu^[51,52] binary collision module already included in the EPOCH code to account for collisions. The collision frequency in EPOCH is calculated for a charged particle α with charge q_α scattering off a charged particle β as follows:

$$\nu_{\alpha\beta} = \frac{(q_\alpha q_\beta)^2 n_\beta \ln(\Lambda)}{4\pi(\epsilon_0 \mu)^2} \frac{1}{v_r^3}, \quad (4)$$

where n_β is the density (for particles of species β), $\ln(\Lambda)$ is the Coulomb logarithm, $\mu = m_\alpha m_\beta / (m_\alpha + m_\beta)$ is the reduced mass and v_r is a relative velocity^[31]. EPOCH extends the model to low temperatures following an approach by Pérez *et al.*^[51] and Lee and More^[53]. More details can be

found in the work of Arber *et al.*^[31] and in the source files and documentation provided with the open-source EPOCH code (<https://epochpic.github.io/>). Collisions are included between all charged particles in the simulation. The Coulomb logarithm is calculated automatically with a fixed lower bound of 1.

EPOCH includes a collisional ionization routine designed for atoms^[31,54], but this is not well suited for impact ionization in dielectrics. A more appropriate ionization rate for our regime can be calculated with the approach by Keldysh^[55], although some of the input parameters to the models are not well reported and may require fitting of output results to experimental data^[41,56]. Impact ionization is reduced for shorter few-cycle pulses. Models by Petrov and Davis^[57] suggest collisional ionization dominates photoionization for fluences exceeding 0.4 J cm^{-2} , whereas the multiple-rate-equation (MRE) model by Rethfeld^[58] predicts this threshold to be 10 J cm^{-2} ^[49]. For this work, we do not include impact ionization, since we model few-cycle pulses that are only 7 fs (fewer than three laser cycles) full width at half maximum (FWHM) in duration. We find good agreement with previous experiments without the need for impact ionization, but expect this to be an important consideration for longer pulses in future work.

2.3. Refraction

The optical properties of dielectrics are modeled using a spatially varying permittivity ϵ throughout the simulation box. At the beginning of the simulation the optical properties are stored in a matrix with the same size as the simulation grid. We then modified the field solver to include a spatially dependent permittivity when advancing Maxwell's equations, following a similar approach to that in the WarpX code^[46] and the modification to EPOCH by Charpin *et al.*^[41]. To easily account for arbitrary target structures, we define the shape of the optical region at the same place where particle species are initialized. There has been work including nonlinear optical effects in PIC and FDTD simulations^[36,59], although those effects are not considered here.

3. Simulation setup

We begin by applying this simulation framework to a slab of fused silica (SiO_2) corresponding to the experiment discussed by Chimier *et al.*^[16] and then apply the framework to a multi-layer mirror, as shown in Figure 1. We test a range of fluences near the reported damage threshold, where the fluence is given by $F = 2E_{\text{las}}/\pi\omega_0^2$, with E_{las} being the energy of the laser pulse. The laser is introduced as a boundary condition and enters into vacuum before interacting with a slab of fused silica at normal incidence. For both the bulk and multi-layer targets, a $\lambda = 800 \text{ nm}$, $\tau_{\text{FWHM}} = 7 \text{ fs}$ pulse

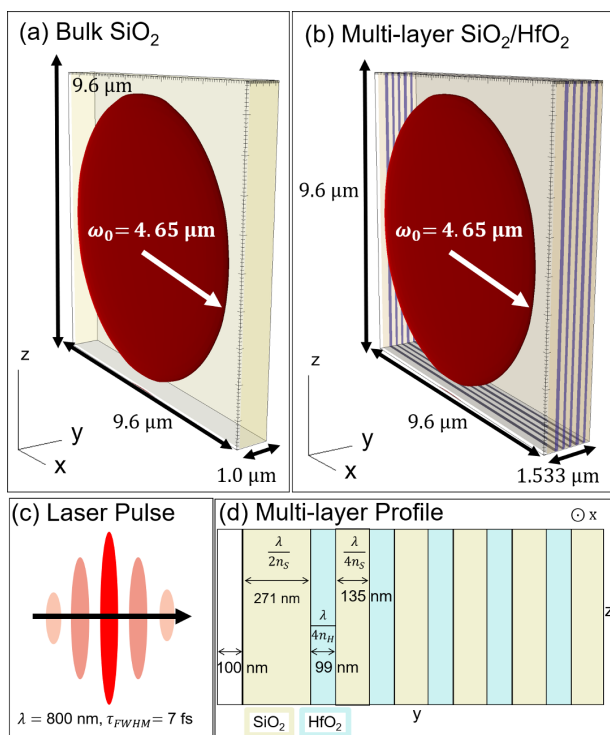


Figure 1. A schematic of the 3D simulations for bulk fused silica (a), and the coating of the multi-layer quarter-wave mirror with a fused SiO₂ protective layer (b). The normally incident few-cycle laser pulse (c) is driven from the minimum y boundary into a 0.1 μm vacuum region before the target. The SiO₂ regions are represented in yellow and the HfO₂ in blue. A cross-section of the multi-layer mirror in the $x-z$ plane is shown in (d) (the z dimension is not to scale). The thickness of the top SiO₂ layer is 270.90 nm and then there are alternating layers of HfO₂ (98.95 nm) and SiO₂ (135.45 nm).

duration, sine-squared pulse with a spot radius of $\omega_0 = 4.65 \mu\text{m}$ is modeled.

3.1. Grid and particle initialization

The simulation setup for bulk SiO₂ is shown in Figure 1(a). The simulation box is 1.0 μm in the longitudinal (y) direction and 9.6 μm in the transverse (x/z) directions. The target is 0.9 μm thick, leaving a 0.1 μm vacuum region before the laser interacts with the target. Simple outflow boundaries are used to allow transmission of the laser out of the simulation box with minimal reflection. The bulk silica simulations have a resolution of 5 nm in the longitudinal (y) direction and 40 nm in the transverse directions. A higher resolution was used in the longitudinal direction to better resolve the ionization dynamics at the interface between the target surface and the vacuum region.

Then we apply this framework to multi-layer interference coatings composed of alternating fused SiO₂ (yellow) and HfO₂ (blue) layers, as shown in Figures 1(b) and 1(d). The simulation space is 9.6 μm by 1.533 μm by 9.6 μm long in the x , y and z directions, respectively, with a resolution of

Table 1. Material properties used in simulations.

Material	Band gap (eV)	Index n	Density (g cm^{-3})	m_h^*	m_e^*
SiO ₂	9 ^[26]	1.477	2.2 ^[62]	8 ^[63]	0.6 ^[63]
HfO ₂	5.7 ^[64]	2.021	9.68	1.12 ^[64]	1.09 ^[64]

13.8 nm in the longitudinal (y) direction and 40 nm in the transverse directions. The thickness of the surface protective SiO₂ layer is $\lambda/(2n)$, while the rest of the layer thickness is $\lambda/(4n)$, a typical Bragg quarter-wavelength mirror, where n is the index of refraction for each material. The top fused SiO₂ layer is placed at 0 μm and the pulse enters normally from the y -axis at $-0.1 \mu\text{m}$.

Both series of simulations are initialized with 1000 neutral SiO₂ (or HfO₂) macroparticles per cell with a temperature of 300 K. Similar to Charpin *et al.*^[41], we found that a large number of particles per cell were required for accuracy with the Keldysh ionization model in this regime. The simulations are run to a simulation time of 24 fs, which allows the pulse to make multiple passes across the simulation domain. For each simulation, we use the default time step in EPOCH of 0.95 times the Courant–Friedrichs–Lewy (CFL) limit^[60,61], or $0.95 / \left(c \sqrt{1/\Delta x^2 + 1/\Delta y^2 + 1/\Delta z^2} \right)$, where Δx , Δy and Δz represent the grid size in each simulation dimension^[31].

3.2. Material properties

The simulations require a number of material properties as inputs to model the interaction and interpret the predictions. These include the linear refractive index, density, and band gap, for which we use standard values listed in Table 1. There is less agreement in reported values for the effective electron and hole masses (m_e^* and m_h^* , respectively) and subsequently this results in different reduced effective masses $m^* = 1 / (1/m_e^* + 1/m_h^*)$. This variation leads to significant differences in predictions for the excited electron density using the Keldysh ionization model^[27,65]. To calculate m_e^* for fused HfO₂, we assume it is the spherically averaged effective mass around the Γ and B points of the monoclinic HfO₂^[64,66]. We generally use material properties for m -HfO₂ as those for amorphous HfO₂ are less readily available. These effective electron masses are used for ionized electron particles in the simulations.

4. Damage modeling of the bulk silica target

We benchmark our framework against the experiment by Chimier *et al.*^[16,21], which finds damage with a fluence of 1.18 J cm⁻² and ablation at 1.3 J cm⁻² for a 7 fs FWHM pulse at normal incidence. There is some uncertainty in

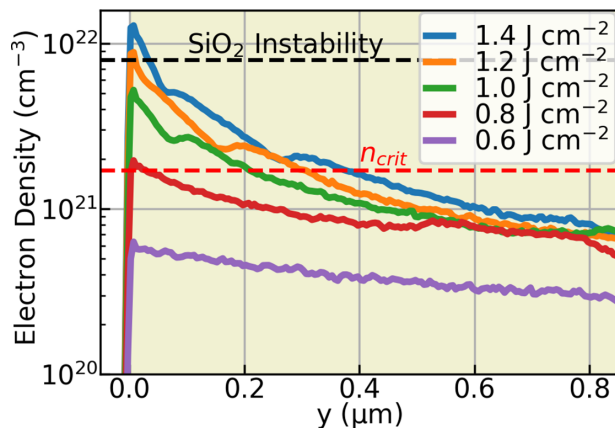


Figure 2. The electron density at the center of the x - z plane (averaged over six cells in x and y) along y at 20 fs for a series of PIC simulations at various laser fluences with a 7 fs duration pulse interacting with bulk SiO₂. The critical plasma density n_{crit} and electron instability density from Ref. [72] are labeled with dashed lines. The latter predicts damage around 1.2 J cm^{-2} .

these thresholds. Other experiments of LIDTs for bulk silica with different experimental conditions including a shorter 5 fs pulse^[15,18] report thresholds from 1.5 to 1.8 J cm^{-2} . We use a 4.65 μm spot radius in our simulations to match the experimental conditions in the work of Chimier *et al.*^[16]. We note that experiments by Lenzner *et al.*^[15] and Kafka *et al.*^[18] used larger spot sizes, although petawatt-class laser systems^[67] can often achieve spot sizes of the order of a few wavelengths (e.g., see Ref. [68]).

4.1. Electron density

For simulation and theoretical work, the predicted excited electron density is often used as a criterion to predict damage. Many studies use the critical electron density^[69] for free electrons or some fraction of total ionization^[70]. This qualitatively makes sense, as exceeding such thresholds can result in high absorption and subsequent damage. This choice has shown good agreement with longer pulses, although recent work has suggested that this description is insufficient for modeling shorter few-cycle pulses^[16,71]. As shown in Figure 2, the damage threshold is predicted at about 0.8 J cm^{-2} by the critical density criterion, which is about a 30% underestimation of the experimental LIDT. Number density is a standard output variable for PIC simulations. It is calculated by mapping the position of the macroparticles to the spatial grid based on the shape function selected for the simulation^[29–31].

Alternatively, the instability density suggested by Stampfli and Bennemann^[72] states that when the conduction band electron density reaches about 9% of the valence band electron density, the elastic shear constant will become negative and the lattice becomes unstable, which then leads directly to a very rapid melting of the crystal structure. This criterion

was developed for crystals, but the fundamental physical principles – namely, the relationship between conduction band electron density and the stability of the atomic structure – are similar. By applying this criterion to the bulk fused SiO₂ simulations, the damage is achieved at about 1.2 J cm^{-2} , which agrees with the experimental results.

4.2. Energy density

The excited electron energy density criterion has also been suggested to predict damage^[71,73]. The predicted energy density is typically compared to material properties, such as the dissociation energy, or an energy barrier associated with melting or boiling^[71,74]. We compare the energy densities in our simulations to these thresholds.

Previous computational approaches typically assume some simple electron energy distribution, whereas in PIC simulation, the energy density can be calculated directly with standard outputs. For our simulations, we multiply the number density by average particle energy for a species in each cell. Alternately, this could be re-sampled to a finer or a coarser grid if the individual macroparticle positions and energies are extracted from the simulation.

Due to variations of reported material properties in the literature and uncertainty of previous simulations, the exact energy density for damage is not agreed upon. For reference, the dissociation energy of SiO₂ has reported values from 54 to 68 kJ cm^{-3} (Refs. [73,75,76]). For comparison, the threshold for high-energy-density physics^[77] is approximately 100 kJ cm^{-3} .

The energy densities related to melting or boiling are lower, where we can use the temperature-dependent heat capacity and latent heat of vaporization used by Zhao *et al.*^[78,79] to calculate an energy density of 5.7 kJ cm^{-3} for melting and 34.7 kJ cm^{-3} for boiling. We do have uncertainty in these values. The latent heat of vaporization has the largest contribution to the boiling criteria and there is a great deal of uncertainty in reported values. For example, the calculation above uses values from Bäuerle^[80], who calculated the latent heat of vaporization of *c*-SiO₂ to be $1.23 \times 10^7 \text{ J kg}^{-1}$, while Kraus *et al.*^[81] reported $(1.177 \pm 0.095) \times 10^7 \text{ J kg}^{-1}$ and Khmyrov *et al.*^[82] used $0.96 \times 10^7 \text{ J kg}^{-1}$ (from Refs. [83,84]). This gives a range from 28.7 to 35.6 kJ cm^{-3} for boiling. We expect some uncertainty in melting energy density as well.

Figure 3 shows the maximum energy density in simulations with and without collisions for a range of laser fluences. The simulations just including photoionization, (without collisions) have lower energy density at the end of the simulation and do not exceed the boiling criterion until much higher fluences are expected for the LIDT in these conditions.

In Figure 3, we see that at 1.3 J cm^{-2} , where ablation is observed in experiments, the simulation energy density

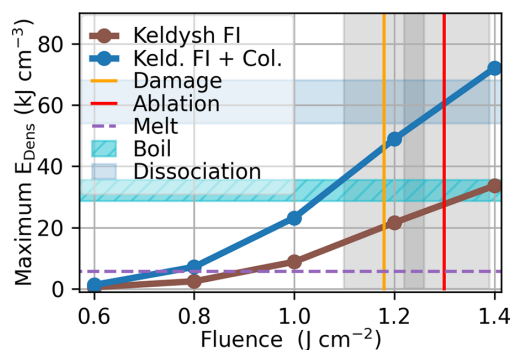


Figure 3. The peak energy density for the series of PIC simulations at various fluences with a 7 fs duration pulse interacting with bulk fused silica. The experiment^[16] being modeled observed damage around 1.18 J cm^{-2} and ablation^[21] at 1.3 J cm^{-2} . The shaded horizontal line/bands indicate approximate energy density thresholds for melting, boiling and dissociation. The shaded vertical bands represent uncertainty in experimental damage and ablation thresholds. The simulations including collisions have a higher predicted energy density. Including both our Keldysh photoionization model and collisional effects shows agreement between the expected damage fluence and the dissociation energy.

overlaps with the reported dissociation energy values. For 1.2 J cm^{-2} , near the LIDT, the energy density for the simulation is around 49 kJ cm^{-3} , exceeding the boiling threshold and near the dissociation energy.

4.3. Kinetic particle motion

The kinetic nature of PIC simulations allows us to explore the energy and motion of the excited electrons. While most previous approaches assume a thermal distribution of the excited electrons, Figure 4 shows that this is not the case

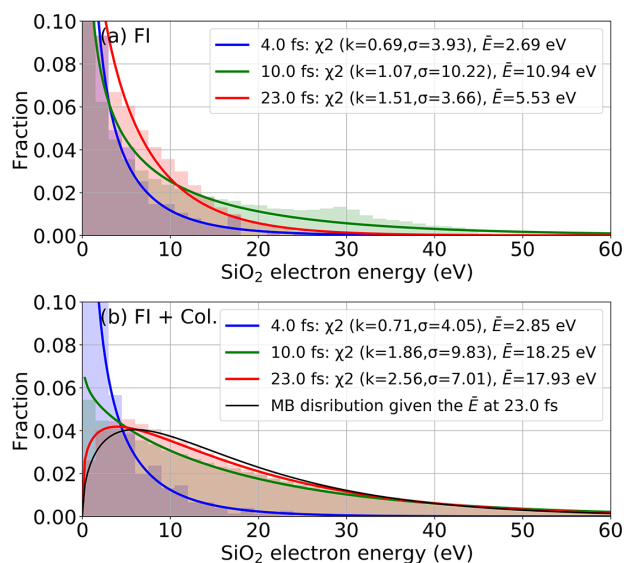


Figure 4. Excited electron energy distributions in a $200 \text{ nm} \times 200 \text{ nm} \times 900 \text{ nm}$ region of the target at the center of the interaction for a 1.2 J cm^{-2} pulse. A simulation with just field ionization is shown in (a) and a simulation with field ionization and collisions is shown in (b). A fit with the given temperature is shown. We observe the nonthermal nature, especially for early times and for simulations without collisions.

during the interaction. The spectra at different times of the simulation are shown and the energy is fitted by the χ^2 distribution using the SciPy^[85] library:

$$\chi^2 : f(E_e; k, \sigma) = \frac{E_e^{k/2-1} e^{-\frac{E_e}{2\sigma}}}{(2\sigma)^{k/2} \Gamma(\frac{k}{2})}, \quad (5)$$

where E_e is the energy of the electrons and fitting parameters k, σ are the degree and scale parameters, respectively. The χ^2 distribution becomes the standard Maxwell–Boltzmann distribution when $k=3$ and $\sigma=k_b T/2$. In our analysis, we primarily focus on the variation of the degrees of freedom k as it is crucial in describing the main characteristics of the Maxwell–Boltzmann distribution. For both cases, with or without collisions, the excited electrons are highly nonthermal at the early stage of 4 fs, where the degree k is about 0.7. Then at 10 fs, after the peak intensity passed through the target, the energy spectrum is still nonthermal with $k=1.07$ when collisions are not included, as shown in Figure 4(a), while in Figure 4(b) the degree k reaches 1.86. At the stable stage of 23 fs, the electrons still remain nonthermal, as shown in Figure 4(a), while in Figure 4(b), the k value is about 2.56, which is approaching the Maxwell–Boltzmann distribution as indicated by the black curve giving the average energy at 23 fs. Therefore, our simulations not only show the dynamic evolution of the excited electron energy spectrum during the interaction but also show the importance of including collisions to capture particle dynamics. When collisions are included in the simulations, the energy absorbed by the electrons increases, leading to higher average energy (Figure 4) and higher maximum energy density (Figure 3) at the end of the simulation.

5. Damage modeling of multi-layer mirrors

For the multi-layer dielectric mirror, HfO_2 is expected to have a lower damage threshold than SiO_2 ^[86,87] due to the lower bandgap. Therefore, the damage may be initiated in the first HfO_2 layer. For example, Talisa *et al.*^[22] found the damage threshold for a four-layer $\text{SiO}_2/\text{HfO}_2$ mirror to be half that of a bulk SiO_2 target. Due to the high computational cost of 3D simulations and uncertainty in material properties for HfO_2 , we explore a simple mirror with a relatively small spot size to gain a better qualitative understanding of the interaction. Future validations with experiments should be coupled with more accurate material property measurements and LIDT measurements of bulk HfO_2 .

5.1. Electron density

As mentioned in Section 4, the plasma critical density may underestimate the damage threshold; it predicts the LIDT slightly above 0.2 J cm^{-2} in the first HfO_2 layer, as shown in Figure 5. If we apply the instability density criterion

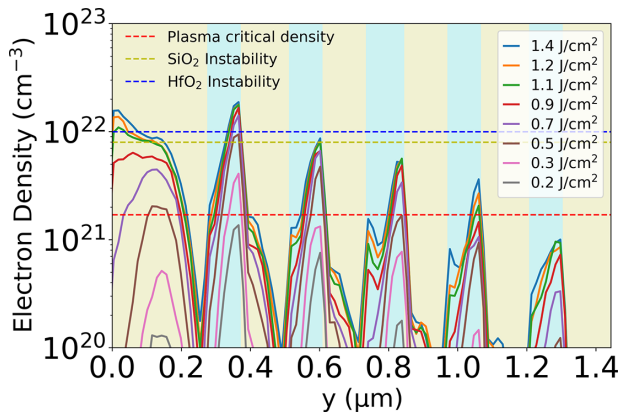


Figure 5. The electron density at the center of the x - z plane along y at 20 fs for a series of PIC simulations at various fluences with a 7 fs duration pulse interacting with a multi-layer mirror. The yellow area is SiO₂ and blue area is HfO₂. Different critical electron densities are labeled in the figure with dashed lines.

to the mirror target, the damage may be achieved at about 0.5 J cm^{-2} in the same layer. Above 0.7 J cm^{-2} , the hot spots in the top two layers are almost fully ionized as the peak electron density reaches about $1.5 \times 10^{22} \text{ cm}^{-3}$.

5.2. Energy density

The peak electron energy density along y at the center of the x - z plane in each layer with different fluences is shown in Figure 6. The dissociation energy of fused HfO₂ has not been extensively studied, particularly for amorphous samples, which are expected in these multi-layer coatings. There are reported values for the formation energy density of m -HfO₂ from 48.44 to 52.64 kJ cm^{-3} [88–94], which are similar to the dissociation energy density of SiO₂. We assume it has the same value as fused SiO₂ since both of their molecules have four valence band electrons and are amorphous[28], which is about 54 kJ cm^{-3} , indicated by the red dashed line. In addition, the effects of structure on boiling and melting points are not considered, as each layer is assumed to retain the melting and boiling points characteristic of its bulk state. This criterion suggests the damage should occur at the surface at fluence of about 1.4 J cm^{-2} , which is even higher than the LIDT of bulk fused SiO₂ discussed in Section 4.

Instead let us consider energy density thresholds for melting and boiling, as these may relate to damage within the layers of a coating. To calculate the melting and boiling energy densities, we make the following assumptions: (i) the vaporization latent heat for HfO₂ is the same as that of SiO₂ and (ii) the heat capacity for fused HfO₂ is the same as that of m -HfO₂[95]. These approximations give the boiling energy density of HfO₂ to be about 49.9 kJ cm^{-3} , which is much higher than that of SiO₂, 34.7 kJ cm^{-3} , and may overestimate the actual damage threshold. Similarly, the melting energy density of SiO₂ is about 5.7 kJ cm^{-3} , and we calculated about 10.7 kJ cm^{-3} for HfO₂.

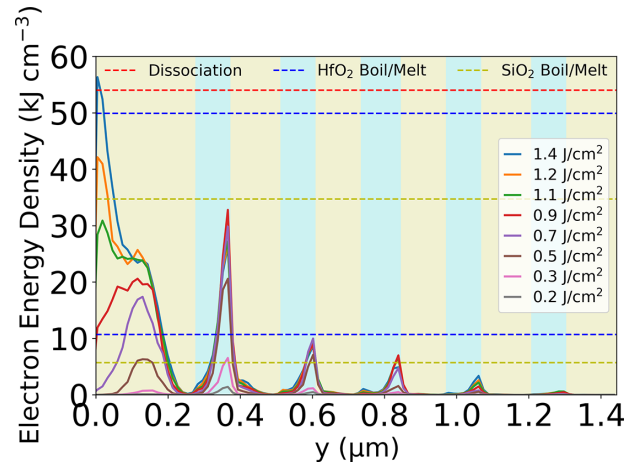


Figure 6. The peak electron energy density at the center of the x - z plane along y at 20 fs for a series of PIC simulations at various fluences with a 7 fs duration pulse interacting with a multi-layer mirror. The yellow area is fused SiO₂ and blue area is fused HfO₂. The SiO₂ boiling and melting energy densities are at about 34.7 and 5.7 kJ cm^{-3} , respectively, indicated as yellow dashed lines, and the HfO₂ boiling and melting energy densities are at about 49.9 and 10.7 kJ cm^{-3} , respectively, indicated as blue dashed lines.

The boiling energy density criterion predicts the LIDT at a fluence between 1.1 and 1.2 J cm^{-2} on the surface of the mirror, which is close to the LIDT of bulk SiO₂. Alternately, applying the melting energy density criterion gives the LIDT to be less than 0.5 J cm^{-2} , and the damage site is initiated in the first HfO₂ layer, as expected.

5.3. Plasma screening effects

As shown in Figure 6, the global maximum energy density at low fluences is in the first HfO₂ layer, as expected. When the fluence exceeds about 1.1 J cm^{-2} it shifts to the top SiO₂ layer and the HfO₂ energy density increases slowly after the fluence reaches about 0.7 J cm^{-2} . This is because the excited electron density in the first SiO₂ layer begins to exceed the critical plasma density (Figure 5). In the top SiO₂ layer, the steady state of the dynamic simulation leads to a local maximum enhancement of the electric field at the center.

As the fluence increases beyond 0.5 J cm^{-2} , we observe a new peak appearing and shifting from the center to the surface in both the electron and energy density profiles. The ionization rate at the center of the top SiO₂ layer is enhanced due to the strong intensity and thus the electron density reaches a maximum. The absorption and reflection will continue to increase so that the source can hardly penetrate the target by the end of the laser pulse. Therefore, the resonant pattern of the electric field is altered, and a new intensity peak appears.

To illustrate this process clearly, a two-dimensional y - z cross-section of the layers at the center of the x -axis is shown in Figure 7 at fluence of 0.7 J cm^{-2} . The maximum electron and energy densities are both observed in the first HfO₂ layer, as shown in Figures 7(a) and 7(b), while the maximum

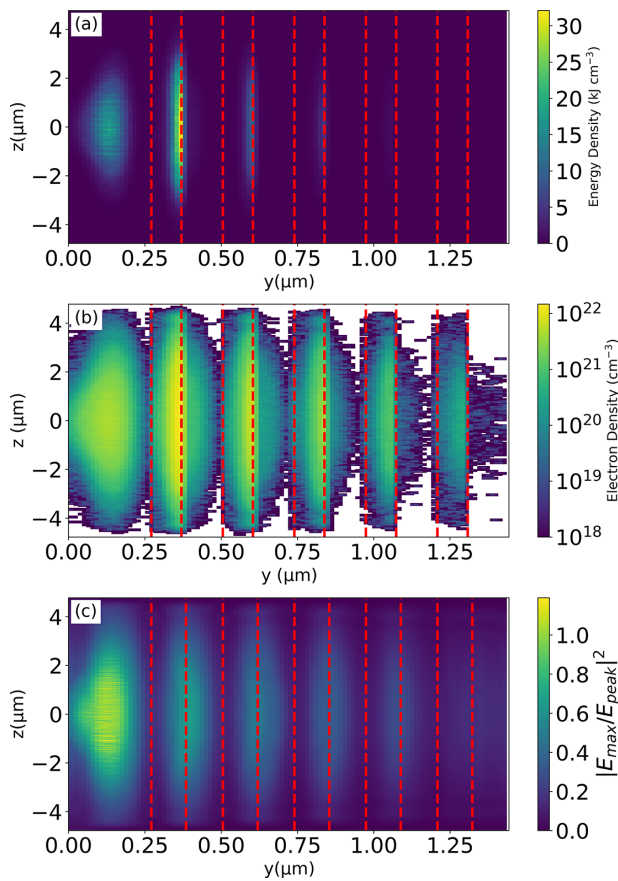


Figure 7. The (a) energy density and (b) electron density at the center of x on the y - z plane at 20 fs and 0.7 J cm^{-2} with a 7 fs duration pulse interacting with a multi-layer mirror. The mirror surface starts at $y = 0$, and the dashed red lines are the interfaces between layers. The white areas have no excited electrons. (c) The maximum accumulated normalized intensity over the entire simulation.

accumulated intensity is in the first SiO_2 layer in Figure 7(c). The intensity is recorded at intervals of 0.5 fs and compared across all time points to generate this figure. These results are similar to those from the FDTD simulations by Zhang *et al.* [28].

Noticeably, the electron density, energy density and intensity profiles in the protective SiO_2 layer all present a bump extending from the center to the surface, which is different from in previous FDTD simulation works by Zhang *et al.* [28]. We observed that the electron density peak first appeared at the center and then expanded at about 9 fs to the surface, and became stable at about 15 fs. These are the times when the pulse peak intensity reached the surface and when the entire pulse left the surface.

Furthermore, in Figure 6, the first HfO_2 layer is more strongly affected by the lower fluence pulse. At higher fluence, there is significant growth of the energy density at the surface, while the lower layers do not show a significant increase. In addition, the energy density at 0.9 J cm^{-2} is the highest among all the fluences, which adds additional

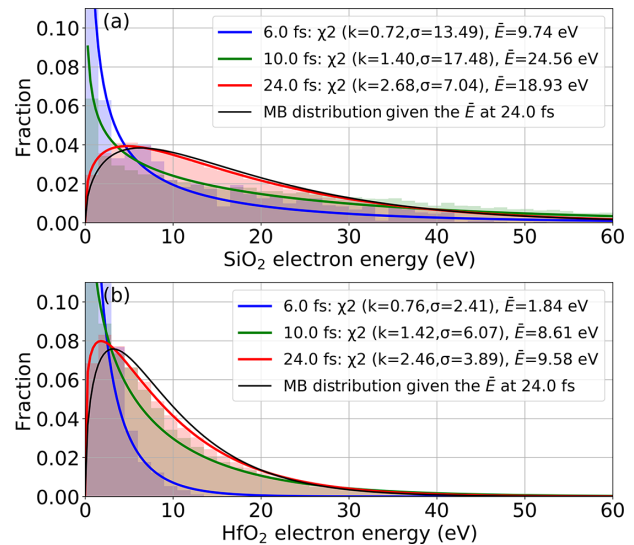


Figure 8. The energy histogram for the electrons in the first SiO_2 layer (a) and HfO_2 layer (b) at 6, 10, 24 fs for the 0.7 J cm^{-2} simulation with χ^2 distribution fitted. The black curve is the Maxwell-Boltzmann distribution given the average energy at the stable stage around 24 fs.

evidence that the first SiO_2 layer has reflected more injected energy due to the plasma screening effects.

The plasma generation could also imply the breakdown threshold, which is defined as a permanent change to the optical properties. We can see from both the energy and electron density profiles that the local peak in the top SiO_2 layer starts to shift at 0.5 J cm^{-2} and the profile is no longer symmetric at the center. This analysis is also consistent with the conclusion predicted by the instability criterion.

5.4. Particle energy

The kinetic nature of the excited electrons is shown in Figure 8. The spectrum of the electrons in the SiO_2 layer is wider than that in the HfO_2 layer, although both electron density and energy density reach maximum in the first HfO_2 layer. For both layers, three snapshots of the energy distribution are shown. At 6 fs, in the early stage of the interaction, there are some excited electrons generated from the ionization. The electrons are highly nonthermalized since the degree k is less than one. At about 10 fs, the peak intensity has passed through the target, leading to average electron energies of 24.56 and 8.61 eV for the SiO_2 and HfO_2 layers, respectively. The electrons are still nonthermalized as k is about 1.4. At 24 fs, the pulse front has left the target for about 10 fs. The degree k is above 2 and approaching 3, indicating the thermalization process is finishing towards a Maxwell-Boltzmann distribution, indicated by the black curves in Figure 8.

5.5. Particle dynamics

The peak intensity of the 0.7 J cm^{-2} pulse is about $10^{14} \text{ W cm}^{-2}$, giving a theoretical ponderomotive energy [96]

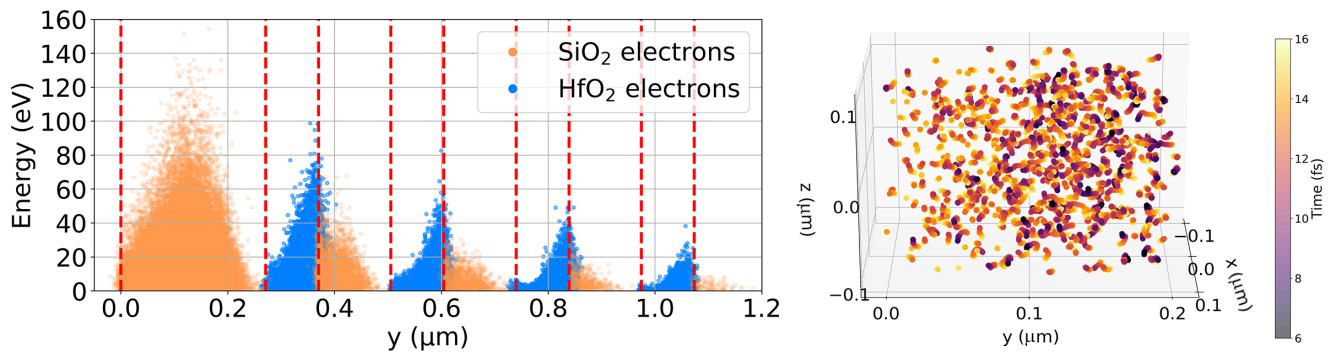


Figure 9. The SiO₂ and HfO₂ electron energy spatial distribution for a fluence of 0.7 J cm^{-2} is shown on the left-hand side at 24 fs. The highest energy particles are found in the center of the first layer and at the interfaces between layers. Particle trajectories for random 2% of electrons with low (below average) final energy demonstrate the ionization dynamics in the first SiO₂ layer up to 16 fs (after the pulse has left). Ionization near the surface generally occurs at later times, as indicated by the color of the tracks.

U_p of approximately 10 and 5.5 eV for SiO₂ and HfO₂ electrons, respectively (using the m_e^* values from Table 1). Some studies have reported keV-scale electron spectra under similar intensities but with longer pulse durations^[96]. This enhancement is often attributed to the surface modification of the target due to ablation, which enhances the local intensity and facilitates stronger electron acceleration. In our previous work, we also observed keV-scale spectra using a 7 fs pulse by introducing pit-like defects on the target surface under comparable conditions^[40].

In gases, electrons with kinetic energies exceeding $10U_p$ are typically observed^[97], and in our simulation, the highest electron energy from the first SiO₂ layer reaches 150 eV. In addition, a few electrons in the first HfO₂ layer achieve energies around 100 eV, as shown in Figure 9 (left). These results align with the kinetic energy predictions for excited electrons based on the Drude model. If we assume the collisional frequency is 1 fs^{-1} , then the energy would be about 118 and 65 eV for SiO₂ and HfO₂, respectively, as seen in the studies by Duchateau *et al.*^[98]. Furthermore, the excited SiO₂ electrons at the HfO₂–SiO₂ interfaces rarely enter the HfO₂ layers. There are a limited number of HfO₂ electrons penetrating into the adjacent SiO₂ layers for a few tens of nanometers.

The tracks of select electrons in the first SiO₂ layer are shown from 6 to 16 fs in Figure 9 (right). Most electrons near the vacuum interface are born after 10 fs, indicated by their yellowish tails. In contrast, electrons near the center of the first SiO₂ layer are born earlier. This suggests that the electron density expansion in Figures 5 and 7(b) is due to direct excitation near the surface rather than displacement from the center.

6. Conclusion

Understanding few-cycle pulse interactions with dielectric optical components and their LIDT is essential for advancing next-generation laser systems. The use of kinetic

simulations in relevant regimes is becoming increasingly popular^[33,36,37,41]. Kinetic simulations allow us to capture the nonthermal nature of the initial interaction, which is important to accurately model absorption and ionization. We show that both excited electron density and energy density provide insight into the LIDT. Our framework shows good agreement with experimental LIDTs for bulk silica targets. Multi-layer mirror simulations indicate that plasma screening effects can alter the laser interaction and electron energy distribution for high fluences.

In the future, this framework can be applied to a variety of mirror and grating designs^[28] for both near- and mid-infrared wavelengths^[39,99]. In addition, simulations can be inserted into an optimization algorithm to optimize the LIDT or other properties of interest for optical components^[100]. This framework already provides a deeper qualitative understanding of the dynamics of laser damage, and we show promising quantitative agreement with experiments for few-cycle pulses. Further development of this framework, including impact ionization^[41,54], coupled with more precise measurements of material properties for relevant optical coating designs, can allow further validation of the framework across large ranges of laser fluence.

Appendix A: Keldysh ionization model implementation

Here we include additional implementation details for our Keldysh ionization model in EPOCH. As stated in Section 2.1, we use 500 terms in the infinite sum in Equation (3). To decide the number of terms, we tested the convergence as shown in Figure 10. Using 100 terms yields errors below 1% for our laser intensities, while selecting 500 terms provided results nearly identical to those for 1000 terms.

The Dawson integral (Φ in Equation (3)) is evaluated using John Burkardt's Fortran 90 code^[101], which is based on the work by Cody *et al.*^[102].

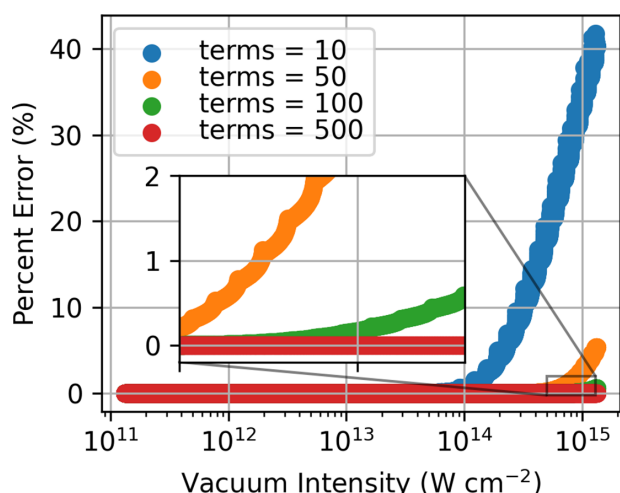


Figure 10. Percent error for 10–500 terms in the infinite sum in Equation (3) for SiO₂ at varying laser intensities. The error is calculated with the result for 1000 terms as the ‘actual’ value. Our simulation framework uses 500 terms, which shows a negligible difference compared to 1000 terms for these intensities. The errors for HfO₂ (not shown) are of similar magnitude to those for SiO₂.

Acknowledgements

This research was funded by DOE STTR grant No. DE-SC0019900. This research used resources of the National Energy Research Scientific Computing Center (NERSC), a Department of Energy Office of Science User Facility using NERSC award SBIR-ERCAP0021422. This project also utilized resources from the Ohio Supercomputer Center^[103]. The code EPOCH used in this work was in part funded by the UK EPSRC grants EP/G054950/1, EP/G056803/1, EP/G055165/1 and EP/M022463/1. This work used matplotlib^[104], SciPy^[85] and NumPy^[105] to graph and analyze the simulation results.

References

- <https://www.nobelprize.org/prizes/physics/2023/press-release/>.
- National Academies of Sciences Engineering and Medicine. *Opportunities in Intense Ultrafast Lasers: Reaching for the Brightest Light* (National Academies Press, 2018).
- R. Falcone, F. Albert, F. Beg, S. Glenzer, T. Ditmire, T. Spinka, and J. Zuegel, [arXiv:2002.09712](https://arxiv.org/abs/2002.09712) (2020).
- M. Ferray, A. L’Huillier, X. F. Li, L. A. Lompre, G. Mainfray, and C. Manus, *J. Phys. B* **21**, L31 (1988).
- P.-M. Paul, E. S. Toma, P. Breger, G. Mullozt, F. Augé, P. Balcou, H. G. Muller, and P. Agostini, *Science* **292**, 1689 (2001).
- M. Hentschel, R. Kienberger, C. Spielmann, G. A. Reider, N. Milosevic, T. Brabec, P. Corkum, U. Heinzmann, M. Drescher, and F. Krausz, *Nature* **414**, 509 (2001).
- T. Brabec and F. Krausz, *Rev. Mod. Phys.* **72**, 545 (2000).
- T. Nagy, P. Simon, and L. Veisz, *Adv. Phys. X* **6**, 1845795 (2021).
- T. Wittmann, B. Horvath, W. Helml, M. G. Schätzel, X. Gu, A. L. Cavalieri, G. G. Paulus, and R. Kienberger, *Nat. Phys.* **5**, 357 (2009).
- F. Mackenroth, A. Di Piazza, and C. H. Keitel, *Phys. Rev. Lett.* **105**, 063903 (2010).
- J. Huijts, I. A. Andriyash, L. Rovige, A. Vernier, and J. Faure, *Phys. Plasmas* **28**, 043101 (2021).
- A. Cavagna, M. Eder, E. Chowdhury, A. Kalouguine, J. Kaur, G. Mourou, S. Haessler, and R. Lopez-Martens, *Opt. Lett.* **50**, 165 (2025).
- B. C. Stuart, M. D. Feit, S. Herman, A. M. Rubenchik, B. W. Shore, and M. D. Perry, *J. Opt. Soc. Am. B* **13**, 459 (1996).
- D. Du, X. Liu, G. Korn, J. Squier, and G. Mourou, *Appl. Phys. Lett.* **64**, 3071 (1994).
- M. Lenzner, J. Krüger, S. Sartania, Z. Cheng, Ch. Spielmann, G. M., W. Kautek, and F. Krausz, *Phys. Rev. Lett.* **80**, 4076 (1998).
- B. Chimier, O. Utéza, N. Sanner, M. Sentis, T. Itina, P. Lassonde, F. Légraré, F. Vidal, and J. C. Kieffer, *Phys. Rev. B* **84**, 094104 (2011).
- M. Lenzner, J. Krüger, W. Kautek, and F. Krausz, *Appl. Phys. A* **68**, 369 (1999).
- K. R. P. Kafka, N. Talisa, G. Tempea, D. R. Austin, C. Neacsu, and E. A. Chowdhury, *Opt. Express* **24**, 28858 (2016).
- N. Sanner, O. Utéza, B. Chimier, M. Sentis, P. Lassonde, F. Légraré, and J. C. Kieffer, *Appl. Phys. Lett.* **96**, 071111 (2010).
- L. Hoffart, P. Lassonde, F. Légraré, F. Vidal, N. Sanner, O. Utéza, M. Sentis, J.-C. Kieffer, and I. Brunette, *Opt. Express* **19**, 230 (2011).
- O. Utéza, N. Sanner, B. Chimier, A. Brocas, N. Varkentina, M. Sentis, P. Lassonde, F. Légraré, and J. C. Kieffer, *Appl. Phys. A* **105**, 131 (2011).
- N. Talisa, A. Alshafey, M. Tripepi, J. Krebs, A. Davenport, E. Randel, C. S. Menoni, and E. A. Chowdhury, *Opt. Lett.* **45**, 2672 (2020).
- M. Kowalczyk, N. Nagl, P. Steinleitner, N. Karpowicz, V. Pervak, A. Gluszek, A. Hudzikowski, F. Krausz, K. F. Mak, and A. Weigel, *Optica* **10**, 801 (2023).
- D. Hui, H. Alqattan, S. Zhang, V. Pervak, E. Chowdhury, and M. Th. Hassan, *Sci. Adv.* **9**, eadf1015 (2023).
- L. Argenti, M. Chini, and L. Fang, *Proceedings of the 8th International Conference on Attosecond Science and Technology* (Springer Nature, 2024).
- J. R. Peñano, P. Sprangle, B. Hafizi, W. Manheimer, and A. Zigler, *Phys. Rev. E* **72**, 036412 (2005).
- S. Zhang, A. Davenport, N. Talisa, J. R. Smith, C. S. Menoni, V. E. Gruzdev, and E. A. Chowdhury, *Proc. SPIE* **11514**, 115141T (2020).
- S. Zhang, C. Menoni, V. Gruzdev, and E. Chowdhury, *Nanomaterials* **12**, 1259 (2022).
- C. K. Birdsall and A. B. Langdon, *Plasma Physics via Computer Simulation*, Series in Plasma Physics (Taylor & Francis, 2004).
- R. Hockney and J. Eastwood, *Computer Simulations Using Particles* (CRC Press, 1988).
- T. D. Arber, K. Bennett, C. S. Brady, A. Lawrence-Douglas, M. G. Ramsay, N. J. Sircombe, P. Gillies, R. G. Evans, H. Schmitz, A. R. Bell, and C. P. Ridgers, *Plasma Phys. Control. Fusion* **57**, 113001 (2015).
- T. Ziegler, I. Göthel, S. Assenbaum, C. Bernert, F.-E. Brack, T. E. Cowan, N. P. Dover, L. Gaus, T. Kluge, S. Kraft, F. Kroll, J. Metzkes-Ng, M. Nishiuchi, I. Prencipe, T. Püschel, M. Rehwald, M. Reimold, H.-P. Schlenvoigt, M. E. P. Umlandt, M. Vescovi, U. Schramm, and K. Zeil, *Nat. Phys.* **20**, 1211 (2024).
- R. A. Mitchell, D. W. Schumacher, and E. A. Chowdhury, *Opt. Lett.* **40**, 2189 (2015).
- G. E. Cochran, P. L. Poole, and D. W. Schumacher, *Phys. Plasmas* **26**, 103103 (2019).

35. P. B. Corkum, *Phys. Rev. Lett.* **71**, 1994 (1993).
36. J.-L. Déziel, L. J. Dubé, S. H. Messaddeq, Y. Messaddeq, and C. Varin, *Phys. Rev. B* **97**, 205116 (2018).
37. W. J. Ding, J. Z. J. Lim, H. T. B. Do, X. Xiong, Z. Mahfoud, C. E. Png, M. Bosman, L. K. Ang, and L. Wu, *Nanophotonics* **9**, 3303 (2020).
38. H. T. B. Do, D. W. Jun, Z. Mahfoud, W. Lin, and M. Bosman, *Nanoscale* **13**, 2801 (2021).
39. M. R. Shcherbakov, G. Sartorello, S. Zhang, J. Bocanegra, M. Bosch, M. Tripepi, N. Talisa, A. AlShafey, J. Smith, S. Londo, F. Légaré, E. Chowdhury, and G. Shvets, *Nat. Commun.* **14**, 6688 (2023).
40. J. R. Smith, S. Zhang, V. E. Gruzdev, and E. A. Chowdhury, in *2021 Conference on Lasers and Electro-Optics (CLEO)* (IEEE, 2021), p. 1.
41. P.-J. Charpin, K. Ardaneh, B. Morel, R. Giust, and F. Courvoisier, *Opt. Express* **32**, 10175 (2024).
42. L. V. Keldysh, *JETP* **20**, 1307 (1965).
43. V. E. Gruzdev, *Proc. SPIE* **5506**, 138 (2004).
44. J. R. Smith, C. Orban, N. Rahman, B. McHugh, R. Oropeza, and E. A. Chowdhury, *Phys. Plasmas* **28**, 074505 (2021).
45. H. Burau, R. Widera, W. Hönig, G. Juckeland, A. Debus, T. Kluge, U. Schramm, T. E. Cowan, R. Sauerbrey, and M. Bussmann, *IEEE Trans. Plasma Sci.* **38**, 2831 (2010).
46. L. Fedeli, A. Huebl, F. Boillod-Cerneux, T. Clark, K. Gott, C. Hillairet, S. Jaure, A. Leblanc, R. Lehe, A. Myers, C. Piechurski, M. Sato, N. Zaim, W. Zhang, J.-L. Vay, and H. Vincenti, in *SC22: International Conference for High Performance Computing, Networking, Storage and Analysis* (IEEE, 2022), p. 1.
47. V. E. Gruzdev, *Proc. SPIE* **5647**, 480 (2005).
48. A.-C. Tien, S. Backus, H. Kapteyn, M. Murnane, and G. Mourou, *Phys. Rev. Lett.* **82**, 3883 (1999).
49. P. Balling and J. Schou, *Rep. Prog. Phys.* **76**, 036502 (2013).
50. D. Terzani and P. Londrillo, *Comput. Phys. Commun.* **242**, 49 (2019).
51. F. Pérez, L. Gremillet, A. Decoster, M. Drouin, and E. Lefebvre, *Phys. Plasmas* **19**, 083104 (2012).
52. K. Nanbu and S. Yonemura, *J. Comput. Phys.* **145**, 639 (1998).
53. Y. T. Lee and R. M. More, *Phys. Fluids* **27**, 1273 (1984).
54. S. Morris, T. Goffrey, K. Bennett, and T. Arber, *Phys. Plasmas* **29**, 123907 (2022).
55. L. V. Keldysh, *JETP* **21**, 1135 (1965).
56. J.-L. Déziel, L. J. Dubé, and C. Varin, *Phys. Rev. B* **104**, 045201 (2021).
57. G. M. Petrov and J. Davis, *J. Phys. B* **41**, 025601 (2008).
58. B. Rethfeld, *Phys. Rev. B* **73**, 035101 (2006).
59. C. Varin, R. Emms, G. Bart, T. Fennel, and T. Brabec, *Comput. Phys. Commun.* **222**, 70 (2018).
60. R. Courant, K. Friedrichs, and H. Lewy, *Math. Ann.* **100**, 32 (1928).
61. R. Courant, K. Friedrichs, and H. Lewy, *IBM J. Res. Develop.* **11**, 215 (1967).
62. W. M. Haynes, *CRC Handbook of Chemistry and Physics*, 93rd edition (Taylor & Francis, 2012).
63. V. A. Gritsenko, R. M. Ivanov, and Y. N. Morokov, *J. Exp. Theor. Phys.* **81**, 1208 (1995).
64. T. V. Perevalov, V. A. Gritsenko, S. B. Erenburg, A. M. Badalyan, H. Wong, and C. W. Kim, *J. Appl. Phys.* **101**, 053704 (2007).
65. V. Gruzdev, *Proc. SPIE* **7842**, 784216 (2010).
66. S. Zhang, M. Tripepi, A. AlShafey, N. Talisa, H. T. Nguyen, B. A. Reagan, E. Sistrunk, D. J. Gibson, D. A. Alessi, and E. A. Chowdhury, *Opt. Express* **29**, 39983 (2021).
67. C. N. Danson, C. Haefner, J. Bromage, T. Butcher, J.-C. F. Chanteloup, E. A. Chowdhury, A. Galvanauskas, L. A. Gizzi, J. Hein, D. I. Hillier, N. W. Hopps, Y. Kato, E. A. Khazanov, R. Kodama, G. Korn, R. Li, Y. Li, J. Limpert, J. Ma, C. H. Nam, D. Neely, D. Papadopoulos, R. R. Penman, L. Qian, J. J. Rocca, A. A. Shaykin, C. W. Siders, C. Spindloe, S. Szatmári, R. M. G. M. Trines, J. Zhu, P. Zhu, and J. D. Zuegel, *High Power Laser Sci. Eng.* **7**, e54 (2019).
68. P. L. Poole, C. Willis, R. L. Daskalova, K. M. George, S. Feister, S. Jiang, J. Snyder, J. Marketon, D. W. Schumacher, K. U. Akli, L. Van Woerkom, R. R. Freeman, and E. A. Chowdhury, *Appl. Opt.* **55**, 4713 (2016).
69. F. F. Chen, *Introduction to Plasma Physics and Controlled Fusion*, 3rd edition (Springer International Publishing, 2016).
70. K. Werner, V. Gruzdev, N. Talisa, K. Kafka, D. Austin, C. M. Liebig, and E. Chowdhury, *Sci. Rep.* **9**, 19993 (2019).
71. P. A. Zhokhov and A. M. Zheltikov, *Sci. Rep.* **8**, 1824 (2018).
72. P. Stampfli and K. H. Bennemann, *Phys. Rev. B* **42**, 7163 (1990).
73. M. Grehn, T. Seuthe, M. Höfner, N. Griga, C. Theiss, A. Mermillod-Blondin, M. Eberstein, H. Eichler, and J. Bonse, *Opt. Mater. Express* **4**, 689 (2014).
74. H. Wang, H. Qi, J. Zhao, B. Wang, and J. Shao, *Opt. Commun.* **387**, 214 (2017).
75. T. Q. Jia, Z. Z. Xu, R. X. Li, D. H. Feng, X. X. Li, C. F. Cheng, H. Y. Sun, N. S. Xu, and H. Z. Wang, *J. Appl. Phys.* **95**, 5166 (2004).
76. S. Inaba, S. Fujino, and K. Morinaga, *J. Am. Ceramic Soc.* **82**, 3501 (1999).
77. R. P. Drake, in *High-Energy-Density Physics* (Springer, 2006), p. 1.
78. J. Zhao, J. Sullivan, J. Zayac, and T. D. Bennett, *J. Appl. Phys.* **95**, 5475 (2004).
79. L. Zhao, J. Cheng, M. Chen, X. Yuan, W. Liao, H. Wang, Q. Liu, and H. Yang, *Results Phys.* **12**, 1363 (2019).
80. D. Bäuerle, *Laser Processing and Chemistry* (Springer Science & Business Media, 2013).
81. R. G. Kraus, S. T. Stewart, D. C. Swift, C. A. Bolme, R. F. Smith, S. Hamel, B. D. Hammel, D. K. Spaulding, D. G. Hicks, J. H. Eggert, and G. W. Collins, *J. Geophys. Res. Planets* **117**, E9 (2012).
82. R. S. Khmyrov, S. N. Grigoriev, A. A. Okunkova, and A. V. Gusarov, *Phys. Procedia* **56**, 345 (2014).
83. I. S. Grigoriev and E. Z. Meilikhov, *Handbook of Physical Quantities* (CRC Press, 1997).
84. G. V. Samsonov, *The Oxide Handbook* (Springer Science & Business Media, 2013).
85. P. Virtanen, R. Gommers, T. E. Oliphant, M. Haberland, T. Reddy, D. Cournapeau, E. Burovski, P. Peterson, W. Weckesser, J. Bright, S. J. van der Walt, M. Brett, J. Wilson, K. J. Millman, N. Mayorov, A. R. J. Nelson, E. Jones, R. Kern, E. Larson, C. J. Carey, I. Polat, Y. Feng, E. W. Moore, J. VanderPlas, D. Laxalde, J. Perktold, R. Cimrman, I. Henriksen, E. A. Quintero, C. R. Harris, A. M. Archibald, A. H. Ribeiro, F. Pedregosa, P. van Mulbregt, and SciPy 1.0 Contributors, *Nat. Methods* **17**, 261 (2020).
86. M. Mero, J. Liu, W. Rudolph, D. Ristau, and K. Starke, *Phys. Rev. B* **71**, 115109 (2005).
87. H. Wang, H. Qi, J. Zhao, B. Wang, and J. Shao, *Opt. Commun.* **387**, 214 (2017).
88. C. Wang, M. Zinkevich, and F. Aldinger, *J. Am. Ceramic Soc.* **89**, 3751 (2006).
89. W. A. Roth and G. Becker, *Z. Phys. Chem.* **159A**, 1 (1932).
90. G. L. Humphrey, *J. Am. Chem. Soc.* **75**, 2806 (1953).
91. E. J. Huber and C. E. Holley, *J. Chem. Eng. Data* **13**, 252 (1968).

92. A. N. Kornilov, I. M. Ushakova, E. J. Huber, and C. E. Holley, *J. Chem. Thermodyn.* **7**, 21 (1975).
93. Y. N. Paputskii, V. A. Krzhizhanovskaya, and V. B. Glushkova, *Inorg. Mater* **10**, 1338 (1974).
94. M. B. Panish and L. Reif, *J. Chem. Phys.* **38**, 253 (1963).
95. J. J. Low, N. H. Paulson, M. D'Mello, and M. Stan, *Calphad* **72**, 11 (2020).
96. G. Geoffroy, G. Duchateau, N. Fedorov, P. Martin, and S. Guizard, *Laser Phys.* **24**, 086101 (2014).
97. G. G. Paulus, W. Becker, W. Nicklich, and H. Walther, *J. Phys. B* **27**, L703 (1994).
98. G. Duchateau, G. Geoffroy, A. Dyan, H. Piombini, and S. Guizard, *Phys. Rev. B* **83**, 075114 (2011).
99. D. R. Austin, K. R. P. Kafka, Y. H. Lai, Z. Wang, C. I. Blaga, and E. A. Chowdhury, *Opt. Lett.* **43**, 3702 (2018).
100. J. R. Smith, C. Orban, J. T. Morrison, K. M. George, G. K. Ngirmang, E. A. Chowdhury, and W. M. Roquemore, *New J. Phys.* **22**, 103067 (2020).
101. <https://github.com/Beliavsky/Burkardt-Fortran-90>.
102. W. J. Cody, K. A. Paciorek, and H. C. Thacher, *Math. Comput.* **24**, 171 (1970).
103. <http://osc.edu/ark:/19495/f5s1ph73>.
104. J. D. Hunter, *Comput. Sci. Eng.* **9**, 90 (2007).
105. C. R. Harris, K. J. Millman, S. J. van der Walt, R. Gommers, P. Virtanen, D. Cournapeau, E. Wieser, J. Taylor, S. Berg, N. J. Smith, R. Kern, M. Picus, S. Hoyer, M. H. van Kerkwijk, M. Brett, A. Haldane, J. F. del Río, M. Wiebe, P. Peterson, P. Gérard-Marchant, K. Sheppard, T. Reddy, W. Weckesser, H. Abbasi, C. Gohlke, and T. E. Oliphant, *Nature* **585**, 357 (2020).